ARL-CR-0834 ● Nov 2018

US Army Research Laboratory

Rietveld Analysis and Simulation of Twinning Effects in Boron Suboxide Powder Diffraction

prepared by W Taylor Shoulders
Oak Ridge Associated Universities
4692 Millennium Dr. #101
Belcamp, MD 21017

under contract W911NF-16-2-0008

Approved for public release; distribution is unlimited.

NOTICES

Disclaimers

The findings in this report are not to be construed as an official Department of the Army position unless so designated by other authorized documents.

Citation of manufacturer's or trade names does not constitute an official endorsement or approval of the use thereof.

Destroy this report when it is no longer needed. Do not return it to the originator.

ARL-CR-0834 ● Nov 2018

US Army Research Laboratory

Rietveld Analysis and Simulation of Twinning Effects in Boron Suboxide Powder Diffraction

prepared by W Taylor Shoulders
Oak Ridge Associated Universities
4692 Millennium Dr. #101
Belcamp, MD 21017

under contract W911NF-16-2-0008

Approved for public release; distribution is unlimited.

REPORT DOCUMENTATION PAGE	*Form Approved* *OMB No. 0704-0188*

Public reporting burden for this collection of information is estimated to average 1 hour per response, including the time for reviewing instructions, searching existing data sources, gathering and maintaining the data needed, and completing and reviewing the collection information. Send comments regarding this burden estimate or any other aspect of this collection of information, including suggestions for reducing the burden, to Department of Defense, Washington Headquarters Services, Directorate for Information Operations and Reports (0704-0188), 1215 Jefferson Davis Highway, Suite 1204, Arlington, VA 22202-4302. Respondents should be aware that notwithstanding any other provision of law, no person shall be subject to any penalty for failing to comply with a collection of information if it does not display a currently valid OMB control number.

PLEASE DO NOT RETURN YOUR FORM TO THE ABOVE ADDRESS.

1. REPORT DATE *(DD-MM-YYYY)* November 2018	**2. REPORT TYPE** Contractor Report	**3. DATES COVERED (From - To)** January–June 2018

4. TITLE AND SUBTITLE Rietveld Analysis and Simulation of Twinning Effects in Boron Suboxide Powder Diffraction	**5a. CONTRACT NUMBER** W911NF-16-2-0008
	5b. GRANT NUMBER
	5c. PROGRAM ELEMENT NUMBER
6. AUTHOR(S) W Taylor Shoulders	**5d. PROJECT NUMBER**
	5e. TASK NUMBER
	5f. WORK UNIT NUMBER
7. PERFORMING ORGANIZATION NAME(S) AND ADDRESS(ES) Oak Ridge Associated Universities 4692 Millennium Dr. #101 Belcamp, MD 21017	**8. PERFORMING ORGANIZATION REPORT NUMBER** ARL-CR-0834
9. SPONSORING/MONITORING AGENCY NAME(S) AND ADDRESS(ES) US Army Research Laboratory ATTN: RDRL-WMM-E Aberdeen Proving Ground, MD 21005-5069	**10. SPONSOR/MONITOR'S ACRONYM(S)** ARL
	11. SPONSOR/MONITOR'S REPORT NUMBER(S)

12. DISTRIBUTION/AVAILABILITY STATEMENT

Approved for public release; distribution is unlimited.

13. SUPPLEMENTARY NOTES

14. ABSTRACT

Boron suboxide (B_6O) ceramics have great potential for use in armor systems. Understanding the structure and defects in armor materials is a major part of developing an understanding of ballistic failure. While much structural characterization effort has been concentrated on the similarly structured boron carbide, still relatively little is known about the defect structures and the subsequent compositional dependence (i.e., boron/oxygen ratio) for B_6O. Rietveld refinement of powder diffraction data is evaluated as an efficient method for structural analysis of B_6O. This report includes examples to assist in setting up a Rietveld refinement of B_6O on the General Structure and Analysis Software. Some more-advanced features, such as the use of Fourier maps to locate potential atomic sites within a unit cell, are also covered. A method for simulating the effect of twins on diffraction patterns is presented. The results of these simulations provide evidence, for the first time, that twinning in B_6O contributes to broad features as well as variations in relative peak intensities.

15. SUBJECT TERMS

boron suboxide, stoichiometry, defects, twinning, Rietveld

16. SECURITY CLASSIFICATION OF:			**17. LIMITATION OF ABSTRACT**	**18. NUMBER OF PAGES**	**19a. NAME OF RESPONSIBLE PERSON**
					W Taylor Shoulders
a. REPORT	**b. ABSTRACT**	**c. THIS PAGE**	UU	33	**19b. TELEPHONE NUMBER (Include area code)**
Unclassified	Unclassified	Unclassified			410-306-0762

Standard Form 298 (Rev. 8/98)
Prescribed by ANSI Std. Z39.18

Contents

List of Figures

List of Tables

Approved for public release; distribution is unlimited.

Acknowledgments

The author would like to acknowledge Dr Kristopher Behler for providing the hot-pressed B_6O–5-v% SiO_2 sample; Howard Payne for providing the sample analyzed in Section 2; and Dr Kristopher Behler and Dr Christopher Marvel for providing the BF ac-STEM image used in Fig. 2 of the report.

1. Introduction

Boron suboxide (B_6O) is a potential high-hardness, low-density armor ceramic. In the past few years, the US Army has focused on hot-pressing small-batch powders, in-house powders synthesized through the oxidation of amorphous boron,[1] and mixtures of elemental boron and boron oxide (B_2O_3). More-recent studies have also involved the use of glassy additives, such as silicon dioxide (SiO_2) and rare-earth oxides, to improve the densification and control grain boundary complexion transitions for property modification.[2] Although B_6O has been of interest to the military for decades[3] and its existence known for even longer,[4] there are still relatively few studies dedicated to understanding the structure and chemistry of B_6O. The boron carbide (B_4C) structure, however, has been studied extensively by methods including nuclear magnetic resonance (NMR),[5,6] vibrational spectroscopy,[7,8] X-ray diffraction (XRD),[9] and neutron diffraction. These structural studies are vital to understanding compositional dependence of performance and the mechanism for breakdown in ballistic performance at high loads.[10] Likewise, an understanding of structure–property relations in B_6O must be developed to realize Army goals.

Compared with the reported Vickers hardness of 45 GPa at a load of 0.98 N in single crystals, the reported Vickers hardness of B_6O ceramics is in the range of 25–35 GPa.[11,12] This is quite a large discrepancy. In fact, structural defects in particular are believed to have a major influence on the properties including hardness,[13] toughness, and elastic modulus.[14,15] Although the general structure of B_6O with 12-membered boron icosahedra bridged by two oxygen atoms and arranged within a rhombohedral unit cell (space group $R\bar{3}m$) has been established (Fig. 1), the structure's accommodation of substoichiometric oxygen levels by the formation of point defects has not been given adequate attention. In addition, high prevalence of twinning and stacking faults in B_6O have been observed in the aberration-corrected scanning transmission electron microscope (STEM) under bright field (BF) conditions (Fig. 2). However, no studies have been dedicated to probing twin statistics in the bulk. Even for B_4C, the effect of twins on performance has been given very little attention in the literature.

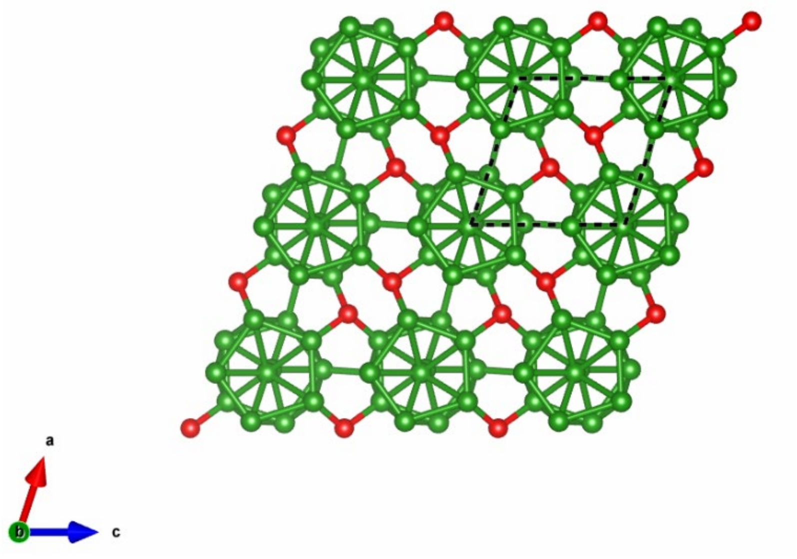

Fig. 1 **Schematic of the B_6O structure with boron atoms in green and oxygen atoms in red**

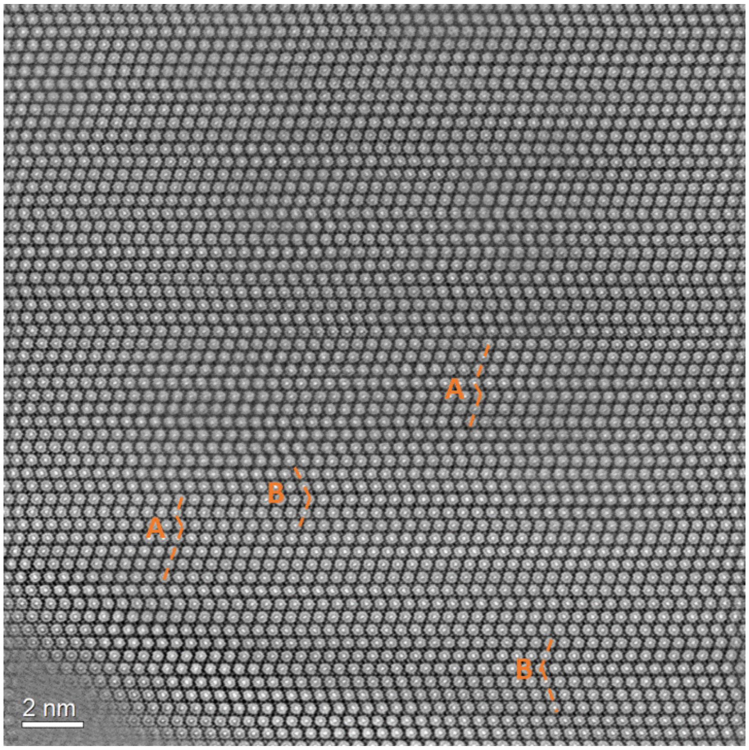

Fig. 2 **Fast Fourier transform–filtered BF-STEM image of a single B_6O grain in a hot-pressed ceramic. Multiple A) stacking faults and B) twins are visible.**

The first step in developing meaningful structure–performance relationships for B_6O is to develop a better understanding of its structure. This report focuses on the use of powder diffraction and Rietveld refinement for determining phase composition,[16] lattice parameters, nonstoichiometry,[17,18] and twinning statistics[19] in

Approved for public release; distribution is unlimited.

B_6O. Similar methods have been used in the past to determine stoichiometry only.[17,20,21] This work set out to establish best practices for Rietveld refinement for the purposes of studying point defects as well as provide some simulations of the effect of twinning on diffraction patterns for the first time.

2. Rietveld Refinement Using GSAS II

The method of Rietveld refinement relies on an iterative nonlinear least-squares algorithm to fit an entire diffraction pattern. Details on the method are covered in Hugo Rietveld's seminal paper from the 1960s.[22] Many modern software packages are available for performing Rietveld analysis. All examples in this report are based on the General Structure and Analysis Software (GSAS) II software developed by Brian Toby and Robert Von Dreele at Argonne National Laboratory.[23] An extensive manual and numerous examples are also available online.[24,25] Although modern software can perform powerful analysis very rapidly, it is important to begin with a few comments on the very basics of Rietveld fitting.

2.1 Software Setup

To account for the instrumental contribution to peak shape, most Rietveld analysis software requires an instrument parameter file including source wavelength, Kα/Kβ intensity ratio, zero offset for the goniometer, and the Gaussian\Lorenztian components to the peak shaping. These are determined by performing a refinement of high-purity Baikalox alpha-alumina powder pattern (Fig. 3) collected on a Bruker D2 Phaser diffractometer with 1.5° soller slits, 0.6-mm divergence slit, and LYNXEYE detector from 10° to 100° 2θ with a step size of 0.02° and an effective collection time of 2 s/step. Figure 4 shows the data contained in the instrument file, which are imported at the start of each refinement. These generic steps for beginning a refinement are covered in more detail in online tutorials.[4]

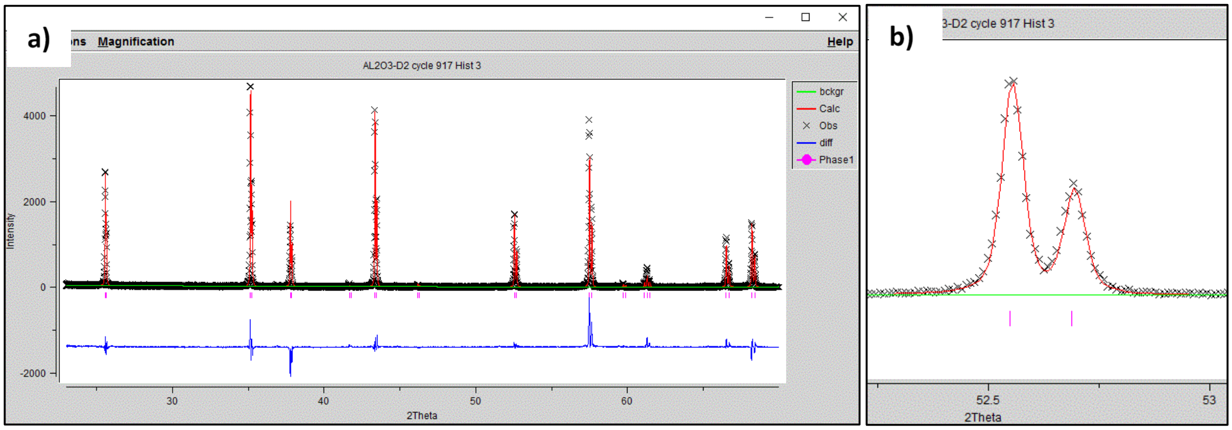

Fig. 3 a) Alpha alumina XRD pattern used for the creation of an instrument parameter file, and b) enhanced view of the 024 peak to show the Rietveld model's good fit to the peak shape

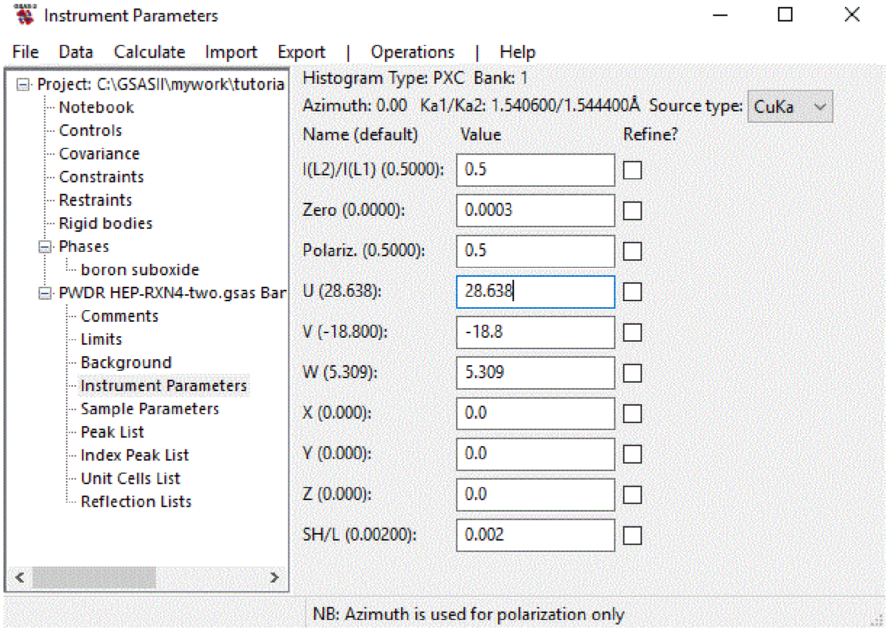

Histogram Type: PXC Bank: 1

Azimuth: 0.00 Ka1/Ka2: 1.540600/1.544400Å Source type: CuKa

Name (default)	Value	Refine?
I(L2)/I(L1) (0.5000):	0.5	☐
Zero (0.0000):	0.0003	☐
Polariz. (0.5000):	0.5	☐
U (28.638):	28.638	☐
V (-18.800):	-18.8	☐
W (5.309):	5.309	☐
X (0.000):	0.0	☐
Y (0.000):	0.0	☐
Z (0.000):	0.0	☐
SH/L (0.00200):	0.002	☐

NB: Azimuth is used for polarization only

Fig. 4 Screenshot showing the instrument parameters for beginning a Rietveld fit

B_6O samples used for the examples in this report were ground to a fine powder with a steel hammer mill and spread in a thin layer over an off-axis silicon holder. Patterns are collected in the same diffractometer configuration (i.e., slits, masks, and the like) as used for the alumina scan described in Fig. 3. The lattice parameters, atomic positions, and isothermal broadening parameters from Olofsson[17] are used as a starting point for refinements.

2.2 General Rietveld Fitting

A pattern collected from a hot-pressed mixture of elemental boron and B_2O_3 is used to demonstrate the basics of Rietveld fitting. The first important step of a profile refinement is to fit a background.

A Chebychev background fitting function with 3–5 terms is used for all examples in this study. An additional complication for B_6O is the presence of broad features centered near 22.2° 2θ and 36.8° 2θ. These so-called amorphous features are modelled as independent background peaks. As the B_6O phase is added, these background peaks are allowed to continuously refine. The background polynomial coefficients and peak parameters are shown in Fig. 5. An impurity peak at 44° 2θ, arising from the steel mill, is added as an excluded region (found in the "Limits" menu). Finally, because the sample sits atop a silicon zero background holder, the sample displacement is refined to account for its effect on peak shift and shape. The results of this first refinement (Calculate>refine) are shown in Fig. 6. The red background curve does a good job approximating the background and amorphous peaks of the blue experimental data. The excluded region is indicated by the purple vertical lines. At this point the peak positions (green lines) are fairly well approximated by the initial structural data; however, the broad peak shapes are not captured. To track the progress of this fit, the weighted R (wR) factor, based on the sum of residuals, is used. The first refinement achieves wR = 15.28%. Typically, a wR less than 10% is considered acceptable; however, chasing a lower wR should be done with caution. Rietveld programs are simultaneously fitting dozens of parameters, which must be kept within physically meaningful bounds.

Approved for public release; distribution is unlimited.

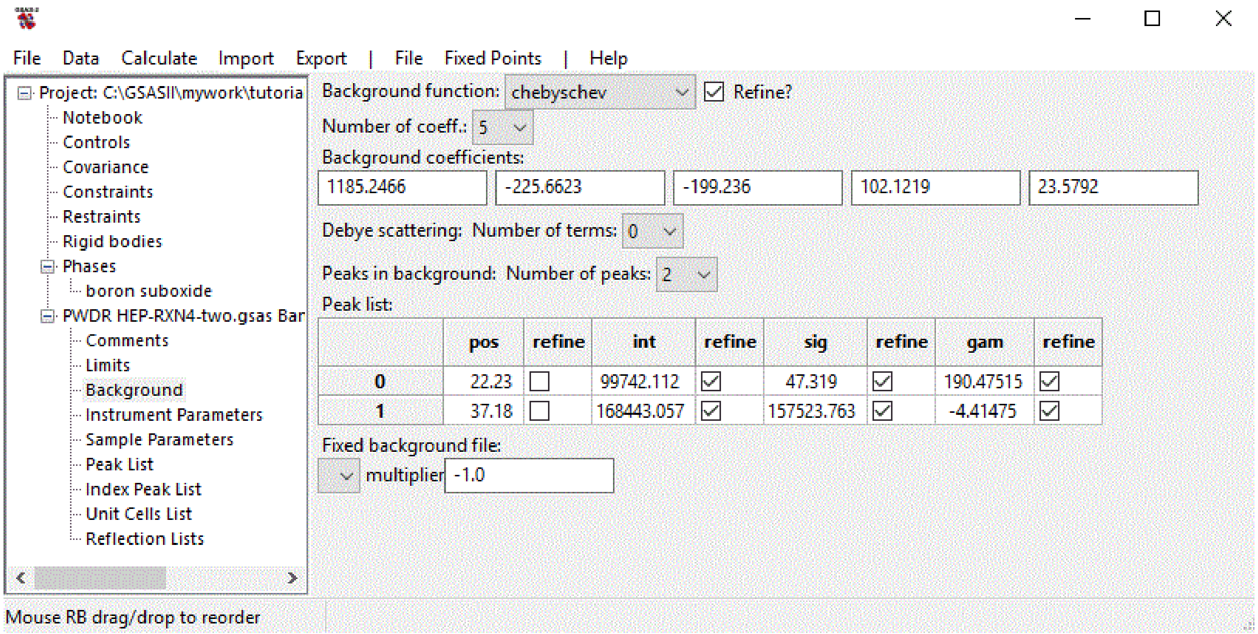

Background function: chebyschev ☑ Refine?

Number of coeff.: 5

Background coefficients:

1185.2466 | -225.6623 | -199.236 | 102.1219 | 23.5792

Debye scattering: Number of terms: 0

Peaks in background: Number of peaks: 2

Peak list:

	pos	refine	int	refine	sig	refine	gam	refine
0	22.23	☐	99742.112	☑	47.319	☑	190.47515	☑
1	37.18	☐	168443.057	☑	157523.763	☑	-4.41475	☑

Fixed background file:

multiplier -1.0

Mouse RB drag/drop to reorder

Fig. 5 Screenshot of the background parameter window showing the five-term Chebyschev function and two independent background peaks

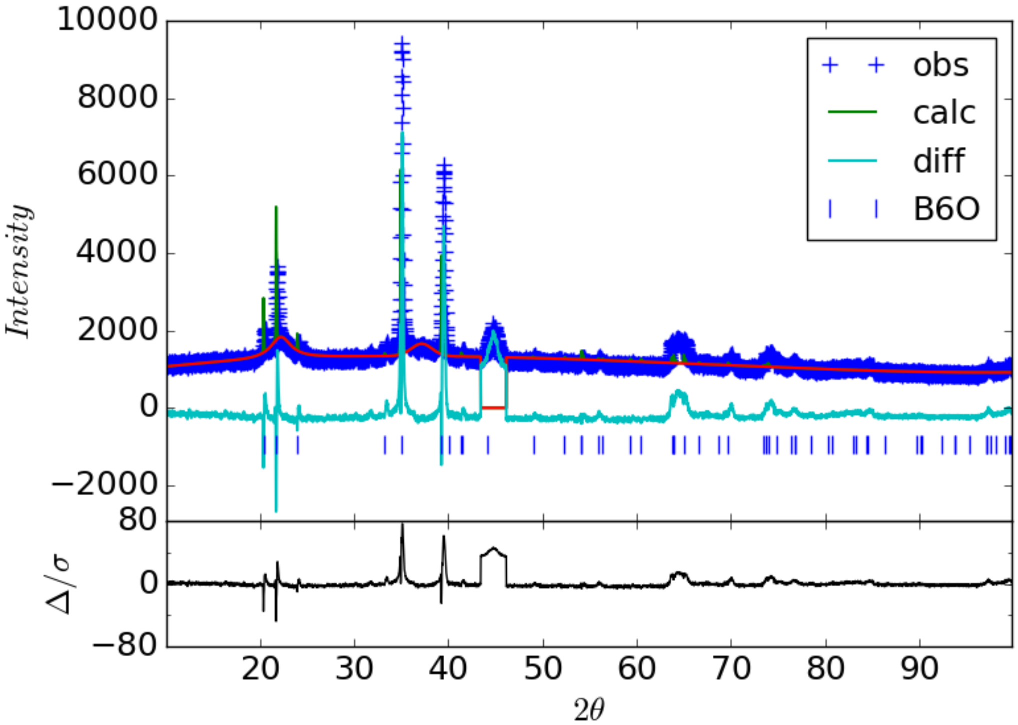

Fig. 6 Screenshot of the first round of fitting (background and sample displacement) for a B_6O sample

In this B_6O sample, because the peak positions are slightly off and the peaks are very broad, a logical next step is to refine lattice parameters and the Lorentzian broadening terms. In GSAS II, the size (microns [µm]) and microstrain checkboxes alter the Lorentzian X and Y terms, respectively, and compute the crystallite size and inhomogeneous strain values based on a Scherrer analysis.[26] The result of the second round of refinement is shown in Fig. 7. The size and strain terms refine to 110 nm and 2200, respectively. The size is physically meaningful based on transmission electron microscopy analysis of similar samples. A strain of 2200 corresponds to a $\Delta d/d$ of 2.2×10^{-3}, also physically reasonable for a low level of residual inhomogeneous strain (from grinding or hot-pressing). After this second refinement, the fitted peak shapes begin to approximate the experimental data; however, the peak intensities are not captured. The wR is 10.90%.

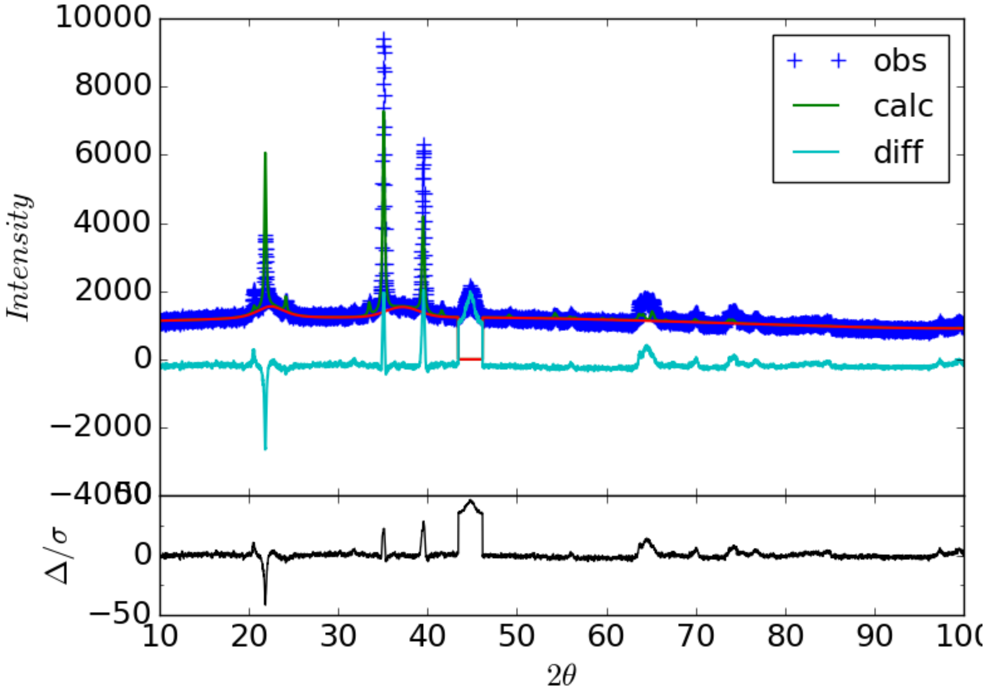

Fig. 7 Result window showing an improved fit after refining lattice parameters and size/strain. The inset shows an enhanced low-angle region to highlight the change in peak shapes in the fitted pattern (green).

In the case of B_6O, one major contributor to incorrect peak intensities is nonstoichiometry.[17,20] To adjust for nonstoichiometry, oxygen site occupancy is altered first. In GSAS II this control is found under the "Atoms" tab within the "Phases" tree item. Here, the x,y,z positions for the three unique atoms in B_6O are listed (Fig. 8). The other refineable fields are the fractional site occupancy (frac.) and isothermal broadening parameter (U_{iso}). The U_{iso}'s account for the thermally activated oscillatory motion of an atom at temperatures above absolute zero.

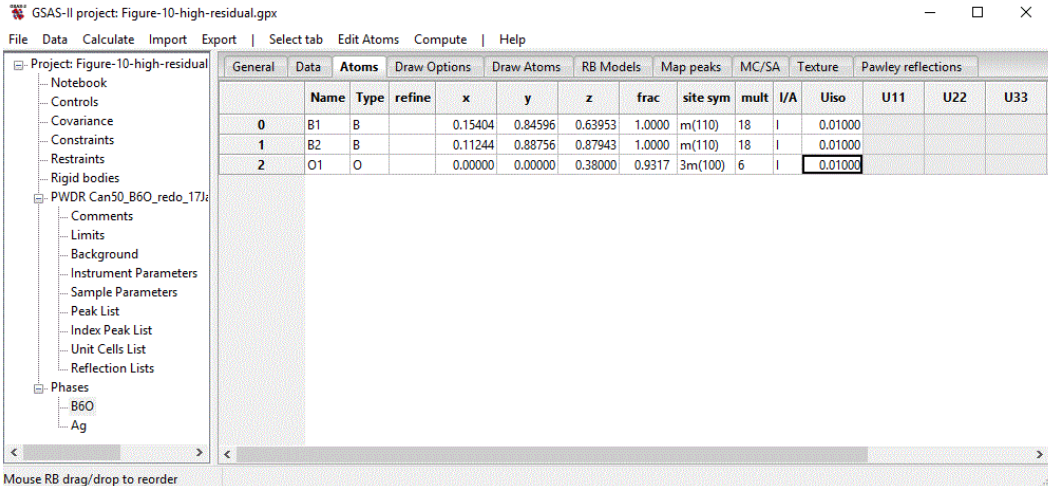

	Name	Type	refine	x	y	z	frac	site sym	mult	I/A	Uiso	U11	U22	U33
0	B1	B		0.15404	0.84596	0.63953	1.0000	m(110)	18	I	0.01000			
1	B2	B		0.11244	0.88756	0.87943	1.0000	m(110)	18	I	0.01000			
2	O1	O		0.00000	0.00000	0.38000	0.9317	3m(100)	6	I	0.01000			

Fig. 8 Screenshot of the "Atoms" data tab, where atomic coordinates, site occupancies, and U_{iso}'s can be viewed and refined

Physically reasonable U_{iso} values for an atom in covalent, inorganic compound are in the neighborhood of 0.01 to 0.04.[27] These are adjusted later in the refinement. However, the frac. for the oxygen atom is refined at this point in the process; the result after another round of refinement is shown in Fig. 9. This fit achieves a wR of 5.662% and corresponds to a frac. of 0.75.

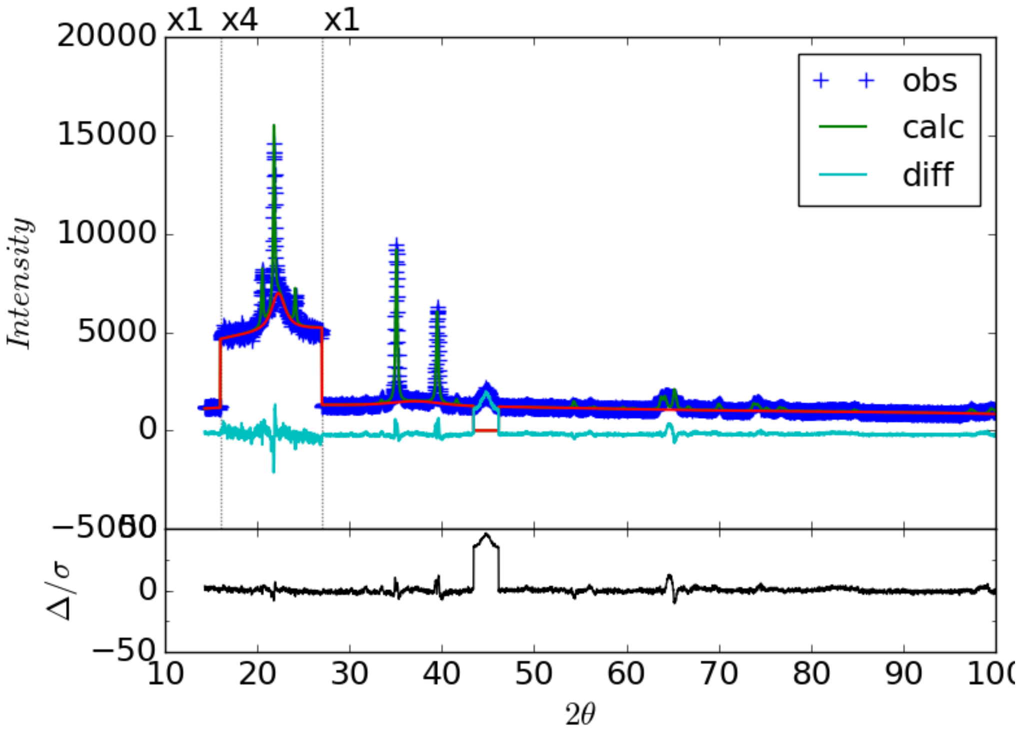

Fig. 9 Result window showing good agreement in peak widths and intensities after refining occupancies

This Rietveld fit assuming oxygen vacancies achieves a very low R-factor, but the question of reasonableness must be raised again. Although it is widely agreed that B_6O can be oxygen-deficient,[17,20,21] the way the structure accommodates this oxygen deficiency is not agreed upon. The presence of boron as a substitutional in the oxygen sites[28] has been proposed in addition to the oxygen vacancy model.[17] Recent G0W0 calculations suggest that both defects should be stable.[29] Unlike boron, there has been no report of "chain" atoms substituting for boron atoms in the B12 icosahedron. Rietveld analysis is certainly not a method to be used exclusively for studying this nonstoichiometry. Quantitative elemental analysis is important to impart some chemical constraint to fits. Methods sensitive to bonding environment, such as X-ray photoelectron spectroscopy (XPS) or NMR would also be complimentary. Nevertheless, the use of Rietveld refinement software to understand this defect structure is demonstrated.

2.3 Advanced Features of Rietveld Refinement

To push the capability of Rietveld refinement further, it is worth taking a closer look at the multiple high-angle residual peaks unattributable to impurity phases that can be found in many samples (Fig. 10). The patterns used in the examples in this section are collected from a hot-pressed B_6O specimen containing 5-v% silica. The entire 3-mm-thick by 25-mm-diameter disc is mounted and scanned to achieve better peak intensities and definitions, especially in the 45° to 60° 2θ range. B_6O has a high X-ray transparency, with an attenuation length of 1.2 mm at 1.54 Å (8.05 MeV). This compares to 84 µm for silicon carbide at the same X-ray energy. Thus, the asymmetry in B_6O peak shape is more pronounced in thicker samples. The asymmetry is incorporated in Rietveld fits by a modified Finger-Cox-Jephcoat model for axial divergence. The attenuation length (centimeters) is entered in the list accessed through the "Sample Parameters" tree item.

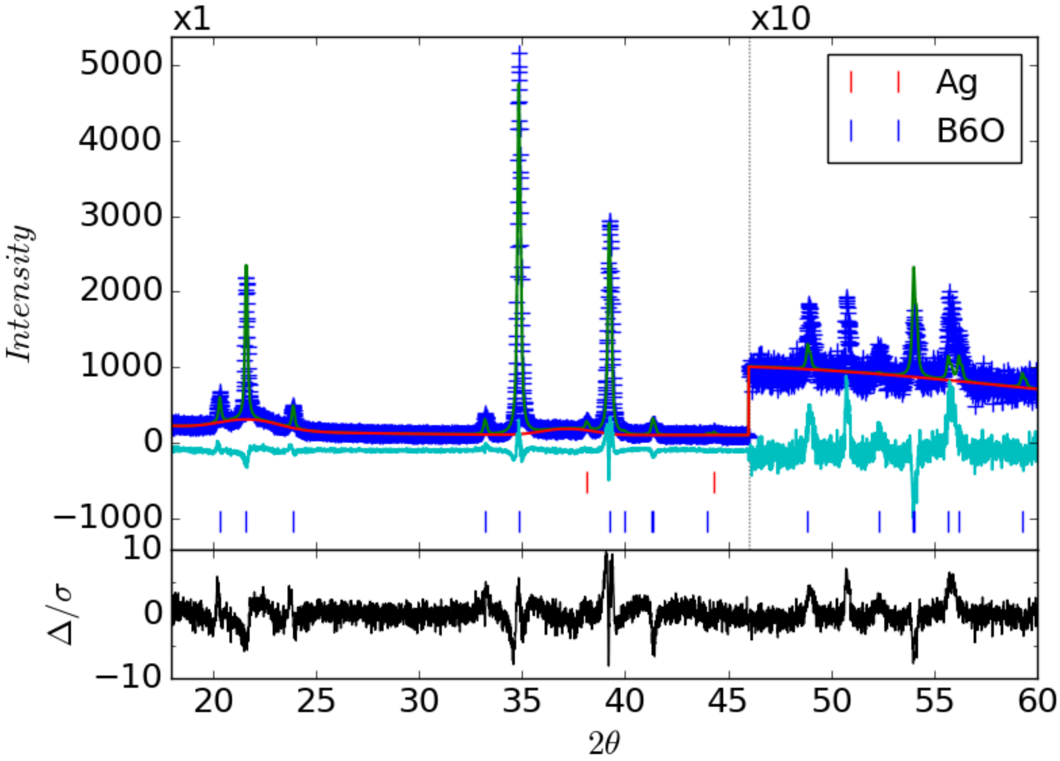

Fig. 10 Rietveld fit in the 48–58 2θ region of a silica-containing B_6O sample showing large residual (green curve)

Now that the refinement incorporates all appropriate peak-shaping models, one approach to finding the source of residual peaks is to transform both the experimental and calculated diffraction patterns into a map of electron density using a Fourier transform, and look for the missing or excess electron density. In GSAS II, this function is found under the "General" tab and "Fourier map controls" (Fig. 11). The "delt-F" or difference Fourier transform, is used for map type. The experimental data used in the calculation are selected by activating the "Select Reflection Sets" button. The spatial resolution and peak cutoff (to set the floor for residual peak intensity and filter out noise) are set to 0.5 and 50, respectively.

Approved for public release; distribution is unlimited.

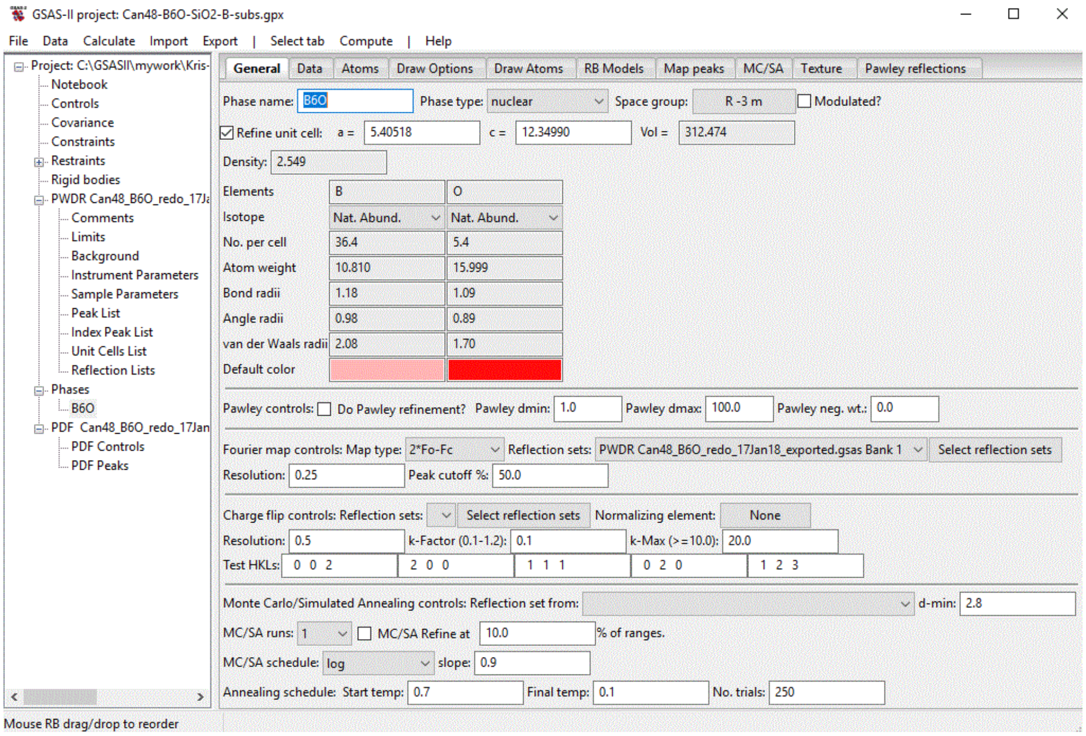

Phase name: B6O Phase type: nuclear Space group: R -3 m ☐ Modulated?

☑ Refine unit cell: a = 5.40518 c = 12.34990 Vol = 312.474

Density: 2.549

Elements	B	O
Isotope	Nat. Abund.	Nat. Abund.
No. per cell	36.4	5.4
Atom weight	10.810	15.999
Bond radii	1.18	1.09
Angle radii	0.98	0.89
van der Waals radii	2.08	1.70
Default color	🟥	🟥

Pawley controls: ☐ Do Pawley refinement? Pawley dmin: 1.0 Pawley dmax: 100.0 Pawley neg. wt.: 0.0

Fourier map controls: Map type: 2*Fo-Fc Reflection sets: PWDR Can48_B6O_redo_17Jan18_exported.gsas Bank 1

Resolution: 0.25 Peak cutoff %: 50.0

Charge flip controls: Reflection sets: Normalizing element: None

Resolution: 0.5 k-Factor (0.1-1.2): 0.1 k-Max (>=10.0): 20.0

Test HKLs: 0 0 2 | 2 0 0 | 1 1 1 | 0 2 0 | 1 2 3

Monte Carlo/Simulated Annealing controls: Reflection set from: d-min: 2.8

MC/SA runs: 1 ☐ MC/SA Refine at 10.0 % of ranges.

MC/SA schedule: log slope: 0.9

Annealing schedule: Start temp: 0.7 Final temp: 0.1 No. trials: 250

Fig. 11 Screenshot of "General" data tab where Fourier map controls are found

To generate the map, "compute>Fourier map" is selected on the top menu bar. The map can be visualized in 3-D using GSAS II, but a second program, VESTA,[30] is used for this task. To save the map, navigate to "ExportMaps as>FOX/Draw XTL file". The map can then be plotted in VESTA along with a .CIF or .str file containing the crystallographic data from the Rietveld fit. Fig. 12 shows the example of the Fourier map visualization corresponding to the pattern in Fig. 10.

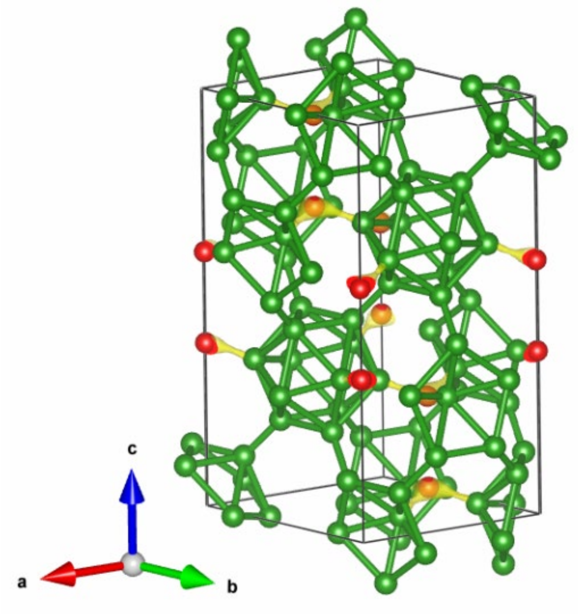

Fig. 12 Difference Fourier map visualization using VESTA. The solid green and red atoms are boron and oxygen, respectively. The translucent yellow regions correspond to the regions missing the most electron density.

From the map it is clear that the areas missing the most electron density (translucent yellow) are slightly off-center from the oxygen site (red sphere). This has been interpreted as evidence of a substitutional with a slightly different position than oxygen it replaces. This site has been found in difference Fourier maps of multiple samples. Possible candidates for occupying this site are boron, silicon, and carbon, a common impurity in samples pressed in graphite dies. The bond length between the new atom and the nearest icosahedral boron (B1 following the nomenclature in Fig. 8) is found to be 1.685 Å compared with 1.499 Å for the B1-O distance. Surveying the literature for bond lengths measured in other icosahedral borides, B-C and B-Si distances are 1.624[9] and 1.973,[31,32] respectively. Because this new distance is very far from published B-Si bond lengths, it is unlikely that silicon occupies this site. The distance is most reasonable for boron (1.65 Å in β-boron[33]), suggesting the presence of boron substitutionals. Based on the position of highest residual density, a boron atom is appended to the position 0, 0, 0.625, and given an occupancy of 0.1. A final refinement on position and occupancy is performed.

The inclusion of boron substitutionals does improve the fit, with only one unidentified peak still remaining at 50.74° 2θ (Fig. 13). The wR has reduced by over 1% after final refinements of positions and U_{iso}'s. The final values of parameters mentioned throughout this fitting are listed in Tables 1 and 2.

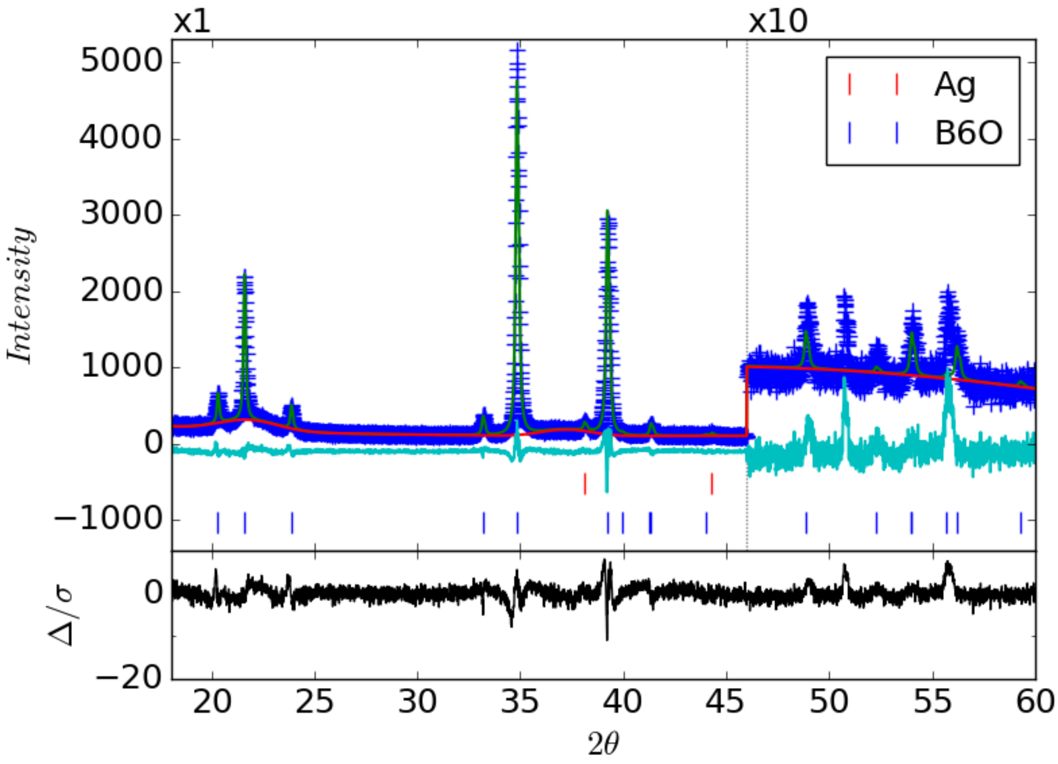

Fig. 13 Rietveld fit in the 48–58 2θ region of a silica-containing B_6O sample showing improved residual (green curve) after incorporation of a substitutional boron atom near the 6c site

Table 1 Atomic parameters upon completion of Rietveld fit for B6O 1v

Atom	x	y	z	occ	U_{iso}
B1	0.1516	0.8486	0.6432	1	0.061
B2	0.1130	0.8870	0.8784	1	0.025
O	0	0	0.3824	0.81	0.012
B3	0	0	0.4294	0.09	0.010

Table 2 Final values for other Rietveld parameters

Parameter	Value	Units
a (hexagonal)	5.398	Å
c (hexagonal)	12.344	Å
Size (Lorentz x)	118	nm
Strain (Lorentz y)	2.5	10^{-3}
Sample displacement	9.21	µm

3. Simulation of the Effects of Twinning

Thus far, the origin of the broad amorphous features modelled as individual peaks in the background has not been discussed. In this section, the possibility of these features arising from twins is explored. B_6O is known to exhibit twins in the $\{0\ \bar{1}\ 1\ 1\}$ family of planes in the hexagonal basis. These have been observed by others[34–37] as well as other work at ARL, as seen in Fig. 2. In addition, density functional theory simulations have identified stable nanotwinned periodic structures.[34] In this section, simulations of random distributions of twins are performed with a program, which recognizes the recurring patterns in randomized stacking sequences to compute the average interference wave function scattered from each layer type occurring in a disordered crystal. A version of this program, first released by Treacy as DIFFAX,[38] is incorporated into GSAS II. To build a layered structure as input to GSAS II, the stacking plane must be perpendicular to the c-axis. This is accomplished by transforming the rhombohedral basis of the B_6O structure by

$$\begin{matrix} 1 & 0 & -0.3113 \\ 0 & 1 & -0.3113 \\ 0 & 0 & 1 \end{matrix} \, . \tag{1}$$

The transformation is performed and visualized using VESTA. Fig. 14 shows two identical structures with ABAB stacking sequence, the first in the rhombohedral basis and the second in the new monoclinic basis. With the structure transformed to an appropriate input format, the "Layers" calculation can now be set up. To distinguish a layered phase, the "phase type" under the "General" tab should be changed from "molecular" to "faulted". At this point, a "Layers" tab should appear along the top of the screen (Fig. 15). The setup continues in this tab. The lattice parameters for the transformed layer structure are entered along with the atomic positions, one by one. A second layer, identical to the first, is created.

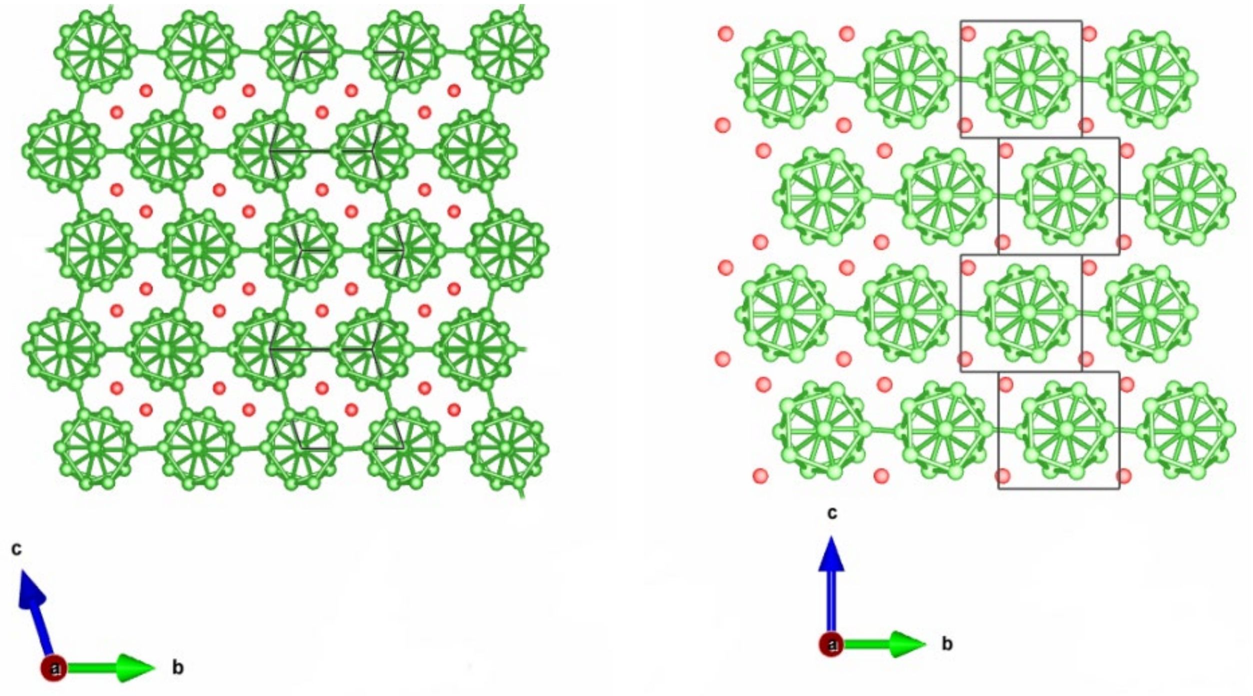

Fig. 14 Representative of ABAB stacking along 001 in a) standard rhombohedral basis and b) new (monoclinic) basis for fault calculations

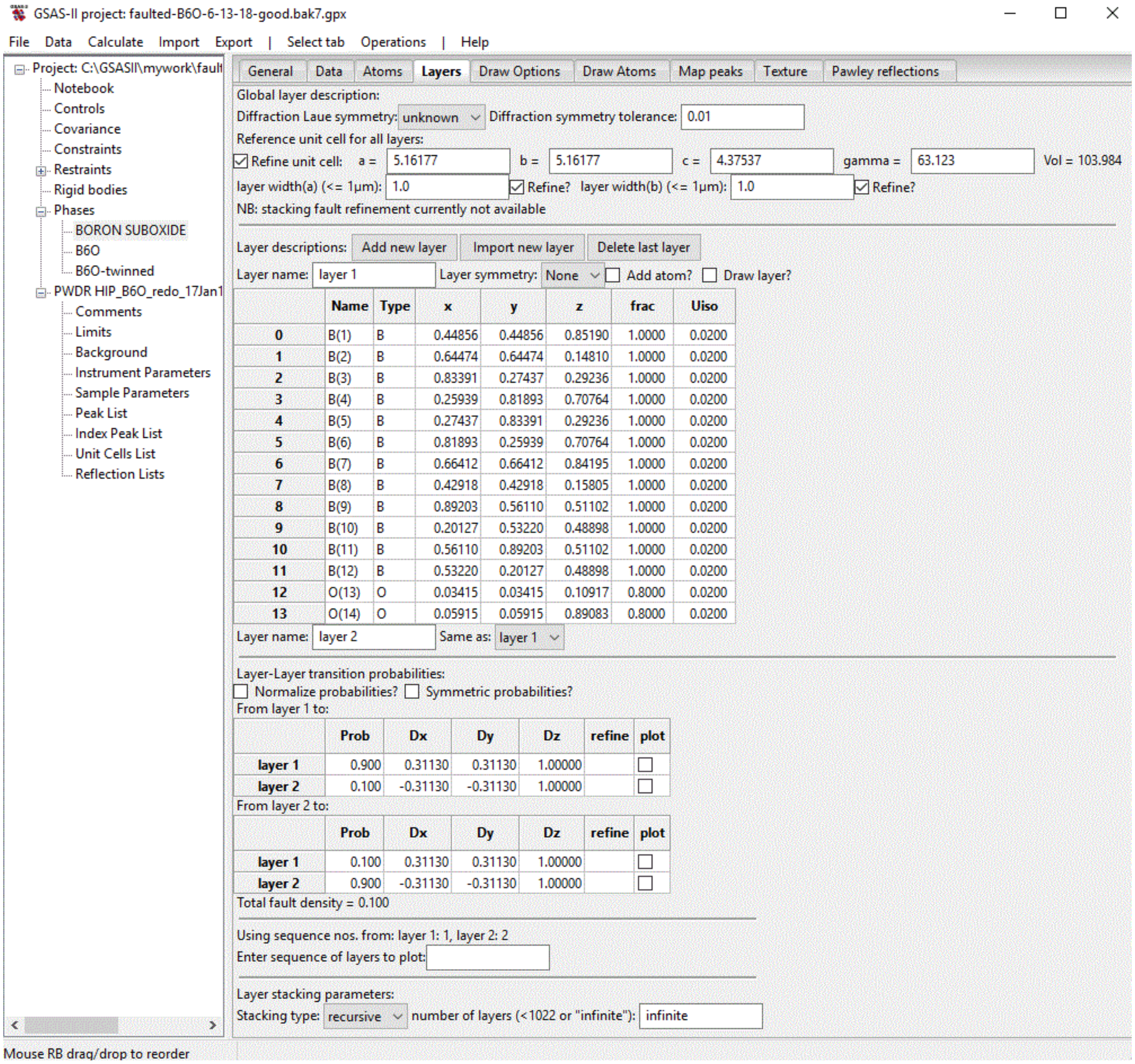

Global layer description:

Diffraction Laue symmetry: unknown Diffraction symmetry tolerance: 0.01

Reference unit cell for all layers:

☑ Refine unit cell: a = 5.16177 b = 5.16177 c = 4.37537 gamma = 63.123 Vol = 103.984

layer width(a) (<= 1μm): 1.0 ☑ Refine? layer width(b) (<= 1μm): 1.0 ☑ Refine?

NB: stacking fault refinement currently not available

Layer descriptions:

Layer name: layer 1 Layer symmetry: None ☐ Add atom? ☐ Draw layer?

	Name	Type	x	y	z	frac	Uiso
0	B(1)	B	0.44856	0.44856	0.85190	1.0000	0.0200
1	B(2)	B	0.64474	0.64474	0.14810	1.0000	0.0200
2	B(3)	B	0.83391	0.27437	0.29236	1.0000	0.0200
3	B(4)	B	0.25939	0.81893	0.70764	1.0000	0.0200
4	B(5)	B	0.27437	0.83391	0.29236	1.0000	0.0200
5	B(6)	B	0.81893	0.25939	0.70764	1.0000	0.0200
6	B(7)	B	0.66412	0.66412	0.84195	1.0000	0.0200
7	B(8)	B	0.42918	0.42918	0.15805	1.0000	0.0200
8	B(9)	B	0.89203	0.56110	0.51102	1.0000	0.0200
9	B(10)	B	0.20127	0.53220	0.48898	1.0000	0.0200
10	B(11)	B	0.56110	0.89203	0.51102	1.0000	0.0200
11	B(12)	B	0.53220	0.20127	0.48898	1.0000	0.0200
12	O(13)	O	0.03415	0.03415	0.10917	0.8000	0.0200
13	O(14)	O	0.05915	0.05915	0.89083	0.8000	0.0200

Layer name: layer 2 Same as: layer 1

Layer-Layer transition probabilities:

☐ Normalize probabilities? ☐ Symmetric probabilities?

From layer 1 to:

	Prob	Dx	Dy	Dz	refine	plot
layer 1	0.900	0.31130	0.31130	1.00000		☐
layer 2	0.100	-0.31130	-0.31130	1.00000		☐

From layer 2 to:

	Prob	Dx	Dy	Dz	refine	plot
layer 1	0.100	0.31130	0.31130	1.00000		☐
layer 2	0.900	-0.31130	-0.31130	1.00000		☐

Total fault density = 0.100

Using sequence nos. from: layer 1: 1, layer 2: 2

Enter sequence of layers to plot:

Layer stacking parameters:

Stacking type: recursive number of layers (<1022 or "infinite"): infinite

Fig. 15 Screenshot of the "Layers" tab used to conduct a twinning simulation in B_6O

The transition vectors (Dx, Dy, Dz) across a twin boundary are entered as seen in Fig. 15. The vector <0.3113 0.3113 1> corresponds to the regular stacking of an untwinned (Layer 1) structure, while <-0.3113 -0.3113 1> corresponds to the formation of a twin. Likewise, in the twinned structure (Layer 2), transitioning along <-0.3113 -0.3113 1> will increase the width of the twin by one layer, while <0.3113 0.3113 1> will transition back to the regular stacking sequence. Thus, altering the 2 × 2 transition matrix between layers will affect the concentration and spacing between twins. A series of simulations is performed, beginning with a Layer 1→1 transition probability of 1 and a Layer 1→2 transition probability of zero. This should approximate an untwinned structure. Ten simulations are performed, keeping the transition matrix symmetric (1→1 = 2→2, 1→2 = 2→1) and normalized (1→1 + 1→2 = 1). The final simulation, where 1→1 and 2→2 are zero, corresponds to a periodic nanotwinned structure called τ-B_6O as suggested by An et. al.[36] The series of 11 successive twin simulations are plotted in Fig. 16.

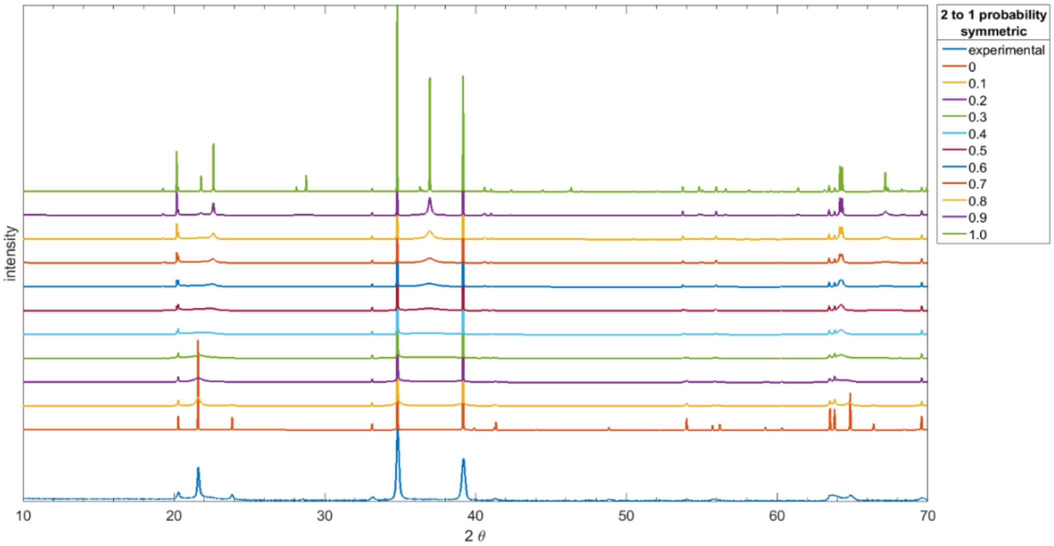

Fig. 16 An experimental B_6O diffraction pattern compared with a series of twinning simulations from 2→1 layer transition probability ranging from 0 to 1. The transition matrix is symmetric (2→1 = 1→2).

From Fig. 16 it is clear that the peak positions of the untwinned simulation (P = 0) approximate those of the experimental pattern. Increasing the transition probability to the alternate layer has the effect of broadening the peaks (P = 0.1, 0.2, and 0.3), especially at 22.2° 2θ. The simulated broadening at 22.2° corresponds to the largest background peak from the Rietveld fits in the previous sections. In addition to peak broadening, additional peaks begin to appear at higher transition probabilities (>0.5) at the positions of 22.64°, 28.78°, 36.97°, 65.4°, and 67.18°. These correspond well to the τ-B_6O pattern simulated by Kunka et. al.[34] Although distinct peaks at these positions are not visible in experimental patterns, the peaks at 36.97° and 65.4° do correspond to an area where a broad background peak is used and a high residual is observed (Fig. 9), respectively. The intensity of the peak at 23.86° decreases very rapidly with increasing transition probability and disappears by P = 2.

To access a larger range of twin spacing, a second round of simulations are performed in which the transition matrix is not symmetric: 1→1 is fixed at 0.95 and 1→2 at 0.05, while 2→2 is varied between 0 and 1. Probabilities remained normalized. The first of these simulations with 2→2 = 0 is considered similar to a bi-crystal with a thick region of Layer 1 followed by a continuous region of Layer 2.

Approved for public release; distribution is unlimited.

The final of these simulations (2→2 = 1) corresponds mostly of Layer 1 with widely spaced one-layer-thick twins. The results of these simulations are plotted in Fig. 17. Here, the rapid decrease of the 23.86° peak and the broadening and disappearing of the 22.2° peak with increasing probability are apparent as in the first set of simulations. In addition, the intensities of the two strongest peaks at 34.8° and 39.2° decrease with increasing transition probability, but show little broadening. These observations suggest that, in addition to stoichiometry, twinning can play a major role in the relative intensities of peaks.

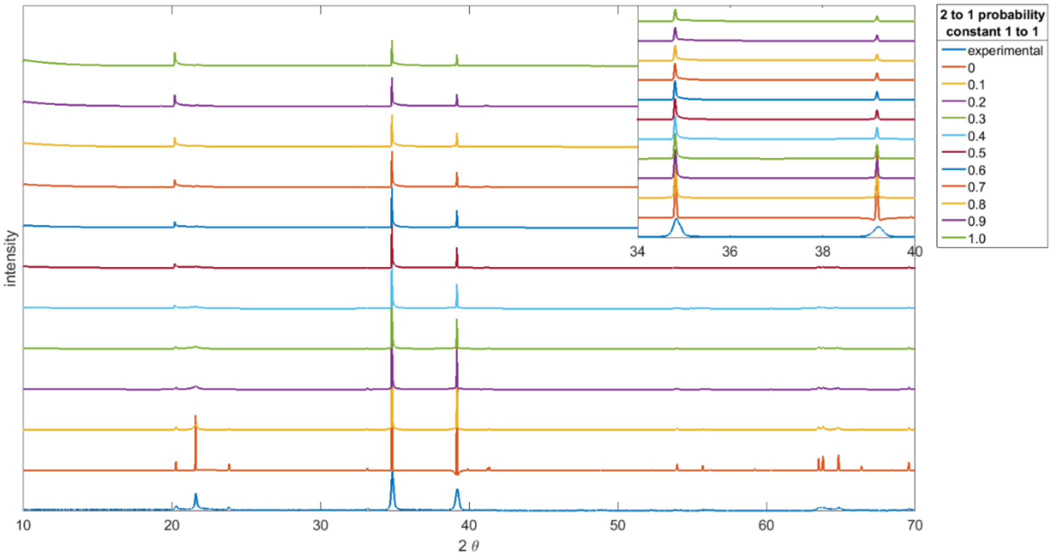

Fig. 17 An experimental B_6O diffraction pattern compared with a series of twinning simulations from 2→1 layer transition probability ranging from 0 to 1. The transition matrix is asymmetric with 1→1 = 0.95 and 1→2 = 0.05 held constant.

Furthermore, the origin of the so-called amorphous features modelled as individual background peaks during Rietveld analysis, is likely twinning. A periodic arrangement of nanotwins in large areas of a sample is unlikely, due to the absence of the extra τ-B_6O peaks in experimental patterns. To predict the concentrations and spacings of twins in samples the simulations will need to be implemented into Rietveld refinements in the future. The simultaneous influence of size/strain broadening, atomic isothermal broadening terms, stoichiometry, and twinning on peak width and intensity are expected to be challenging to decouple.

4. Conclusion

Sections 1 and 2 of this report showed the potential of Rietveld refinement to provide helpful insight into questions of stoichiometry and defect structure in icosahedral borides, especially B_6O. With modern software, the basic fitting procedure is accessible to most analysts. Major pitfalls, such as the account of

Approved for public release; distribution is unlimited.

instrumental parameters, sample displacement, and isothermal broadening terms have been addressed. More-advanced features of Rietveld fitting, such as the use of Fourier maps of electron density to locate atomic positions, have also been covered. The major finding in Rietveld analysis of B_6O samples thus far is the evidence of boron substitutionals on the oxygen site. Advancing further will require additional diffraction methods. For instance, higher-resolution synchrotron data might highlight the subtle changes in peak intensities and shapes needed for determining both site chemistry and occupancy. Furthermore, neutron diffraction may provide overall better scattering efficiency with, unfortunately, no gain in contrast between oxygen and boron. Finally, the use of nondiffraction-based methods such as elemental analysis and defect spectroscopy (i.e., XPS or NMR) will also be complementary.

Section 3 of this report presented simulations on the effect of twinning on diffraction patterns. Results suggest that twins do contribute to the observation of broad diffraction bands in experimental patterns as well as changes in the relative intensities of peaks. These initial results are qualitative, and the goal is for future work integrating the simulations into whole-pattern-fitting algorithms to be more quantitative. This method would provide a more timely analysis of the extent of twinning in a sample. Currently, the only other method is quantitative microscopy, which due to the nanoscale size of the twins, is inaccessible to many research groups.

5. References

1. Pavlacka RJ, Glide GA, inventors; US Army Research Laboratory, assignee. Method for synthesis of boron suboxide. United States patent US 20140227158A1. 2018 Mar 6.

2. Coleman SP, Hernandez-Rivera E, Behler KD, Synowczynski-Dunn J, Tschopp MA. Challenges of engineering grain boundaries in boron-based armor ceramics. JOM. 2016;68:1605–1615.

3. Goosey B, inventor; US Air Force, assignee. Method of fabricating boron suboxide articles. United States patent US 3816586A. 1972 March 21.

4. Pasternak R. Crystallographic evidence for the existence of B7O. Acta Crystallographica. 1959;12:612–613.

5. Pallier C, Leyssale J-M, Truflandier LA, Bui AT, Weisbecker P, Gervais C, Fischer HE, Sirotti F, Teyssandier F, Chollon G. Structure of an amorphous boron carbide film: an experimental and computational approach. Chem Mater. 2013;25:2618–2629.

6. Mauri F, Vast N, Pickard CJ. Atomic structure of icosahedral B_4C boron carbide from a first principles analysis of NMR spectra. Physical Review Letters. 2001;87:085506.

7. Vast N, Lazzari R, Besson JM, Baroni S, Dal Corso A. Atomic structure and vibrational properties of icosahedral α-boron and B_4C boron carbide. Computational Materials Science. 2000;17:127–132.

8. Domnich V, Reynaud S, Haber RA, Chhowalla M. Boron carbide: structure, properties, and stability under stress. J Am Ceram Soc. 2011;94:3605–3628.

9. Sologub O, Michiue Y, Mori T. Boron carbide, B13-xC2-y (x = 0.12, y = 0.01). Acta Crystallographica Section E. 2012;68:i67.

10. LaSalvia JC. Shear localization in a sphere-impacted armor-grade boron carbide. Proceedings of the 23rd International Symposium on Ballistics; 2007 April 16–20; Tarragona, Spain.

11. Thiele M, Herrmann M, Michaelis A. B_6O materials with Al_2O_3/Y_2O_3 additives densified by FAST/SPS and HIP. Journal of the European Ceramic Society. 2013;33:2375–2390.

12. Thiele M, Hermann M, Müller C, Gestrich T, Michaelis A. Reactive and non-reactive preparation of B_6O materials by FAST/SPS. Journal of the European Ceramic Society. 2015;35:47–60.

13. He D, Zhao Y, Zerda TW, Daemen L, Qian J, She TD. Boron suboxide: as hard as cubic boron nitride. Appl Phys Lett. 2002;81:643–645.

14. Kurakevych OO, Solozhenko VL. Experimental study and critical review of structural, thermodynamic and mechanical properties of superhard refractory boron suboxide B_6O. J Superhard Mater+. 2011;33:421–428.

15. Ektarawong A, Simak SI, Hultman L, Birch J, Tasnádi F, Wang F, Alling B. Effects of configurational disorder on the elastic properties of icosahedral boron-rich alloys based on B6O, B13C2, and B4C, and their mixing thermodynamics. J Chem Phys. 2016;14416.

16. Ortiz AL, Sánchez-Bajo F, Padture NP, Cumbrera FL, Guiberteau F. Quantitative polytype-composition analyses of SiC using X-ray diffraction: a critical comparison between the polymorphic and the Rietveld methods. Journal of the European Ceramic Society. 2001;21:1237–1248.

17. Olofsson M, Lundström T. Synthesis and structure of non-stoichiometric B_6O. J Alloy Compd. 1997;257:91–95.

18. Morosin B, Kwei GH, Lawson AC, Aselage TL, Emin D. Neutron powder diffraction refinement of boron carbides nature of intericosahedral chains. J Alloy Compd. 1995;226:121–125.

19. Anselmi-Tamburini U, Ohyanagi M, Munir ZA. Modeling studies of the effect of twins on the X-ray diffraction patterns of boron carbide. Chem Mater. 2004;16:4347–4351.

20. Hubert H. High-pressure, high-temperature synthesis and characterization of boron suboxide (B_6O). Chem Mater. 1998;10:1530–1537.

21. Bills PM, Lewis D. Non-stoichiometry of boron suboxide (B_6O). Journal of Less-Common Metals. 1976;45:343–345.

22. Rietveld H. A profile refinement method for nuclear and magnetic structures. Journal of Applied Crystallography. 1969;2:65–71.

23. Toby BH, Von Dreele RB. GSAS-II: the genesis of a modern open-source all-purpose crystallography software package. Journal of Applied Crystallography. 2013;46:544–549.

24. GSAS-2 wiki [accessed 2018 June]. https://subversion.xray.aps.anl.gov/trac.

25. GSAS-2 tutorials [accessed 2018 June]. https://subversion.xray.aps.anl.gov /pyGSAS/trunk/help/Tutorials.html.

26. Khorsand Zak AA, Majid WH, Abrishami ME, Yousefi R. X-ray analysis of ZnO nanoparticles by Williamson-Hall and size-strain plot methods. Solid State Science. 2011;13:251–256.

27. Kuhs WF. Physical properties of crystals. In: Authier A, editor. International tables for crystallography. Vol. D. Dordrecht (Netherlands): Springer; 2003. p. 228–242.

28. Slack GA, Morgan KE. Some crystallography, chemistry, physics, and thermodynamics of B12O2, B12P2, B12As2, and related alpha-boron type crystals. J Phys Chem Sol. 2014;75:1054–1074.

29. Varley JB, Lordi V, Miglio A, Hautier G. Electronic structure and defect properties of B_6O from hybrid functional and many-body perturbation theory calculations: a possible ambipolar transparent conductor. Phys Rev B. 2014;90:045205.

30. Momma K, Izumi KM. VESTA 3 for three-dimensional visualization of crystal, volumetric and morphology data. J Appl Cryst. 2011;44:1272–1276.

31. Roger J, Babizhetskyy V, Halet J-F, Guérin R. Boron–silicon solid solution: synthesis and crystal structure of a carbon-doped boron-rich SiBn (n~30) compound. J Solid State Chem. 2004;177:4167–4174.

32. Salvador JR, Bilc D, Mahanti SD, Kanatzidis MG. Stabilization of β-SiB3 from liquid Ga: a boron-rich binary semiconductor resistant to high-temperature air oxidation. Angewandte Chemie International Edition. 2003;42:1929–1932.

33. Hughes R, Kennard CHL, Sullenger DB, Weakliem HA, Sands DE, Hoard JL. The structure of β-rhombohedral boron. Journal of the American Chemical Society. 1963;85:361–362.

34. Kunka C, An Q, Rudawski n, Subhash G, Zheng J, Halls V, Singh J. Nanotwinning and amorphization of boron suboxide. Acta Materialia. 2018;147:195–202.

35. An Q, Reddy KM, Qian J, Hemker KJ, Chen M-W, Goddard WA III. Nucleation of amorphous shear bands at nanotwins in boron suboxide. Nature Communications. 2016;7:11001.

36. An Q, Reddy KM, Dong H, Chen M, Oganov AR, Goddard WA III. Nanotwinned boron suboxide (B_6O): new ground state of B_6O. Nano Lett. 2016;16(7):4236–4242.

37. Jiang J, Cao M, Sun Y, Wu P, Yuan J. Star-shaped cyclic-twinning nanowires. Appl Phys Lett. 2006;88:163107.

38. Treacy MMJ, Newsam MJ, Deem MW. A general recursion method for calculating diffracted intensities from crystals containing planar faults. Proceedings of the Royal Society of London. Series A: Mathematical and Physical Sciences. 1991;433:499–520.

List of Symbols, Abbreviations, and Acronyms

µm	micron
3-D	3-dimensional
B_4C	boron carbide
B_2O_3	boron oxide
B_6O	boron suboxide
BF	bright field
frac.	fractional site occupancy
GSAS II	General Structure and Analysis Software II
NMR	nuclear magnetic resonance
SiO_2	silicon dioxide
STEM	scanning transmission electron microscope
U_{iso}	isothermal broadening parameter
wR	weighted R
XPS	X-ray photoelectron spectroscopy
XRD	X-ray diffraction

1 (PDF)	DEFENSE TECHNICAL INFORMATION CTR DTIC OCA
2 (PDF)	DIR ARL IMAL HRA RECORDS MGMT RDRL DCL TECH LIB
1 (PDF)	GOVT PRINTG OFC A MALHOTRA
10 (PDF)	ARL RDRL WM J ZABINSKI RDRL WMM M VANLANDINGHAM RDRL WMM B E HERNANDEZ RDRL WMM E S SILTON L VARGAS-GONZALEZ J LASALVIA K BEHLER S COLEMAN V BLAIR A FRY